



# Deposition of zirconium oxide using atmospheric pressure plasma enhanced chemical vapor deposition with various precursors

Dhruval Patel<sup>a</sup>, Lucia Bonova<sup>a,b</sup>, Zachary Jeckell<sup>a</sup>, D. Eitan Barlaz<sup>a</sup>, Santanu Chaudhuri<sup>c</sup>, Daniel V. Krogstad<sup>d</sup>, David N. Ruzic<sup>a,\*</sup>

<sup>a</sup> Nuclear, Plasma, Radiological Engineering, University of Illinois at Urbana-Champaign, 104 South Wright St., Urbana, IL-61801

<sup>b</sup> Advanced Technologies Research Institute, Slovak University of Technology in Bratislava, Jána Bottu 25, 91724 Trnava, Slovakia

<sup>c</sup> Civil, Materials, and Environmental Engineering, University of Illinois at Chicago, 2095 Engineering Research Facility, 842 W. Taylor St., Chicago, IL-60607

<sup>d</sup> Applied Research Institute, 2100 S. Oak St., Champaign, IL-61820

## ARTICLE INFO

### Keywords:

Atmospheric pressure plasma

Zirconia

Liquid assisted plasma enhanced chemical vapor deposition

Zirconium oxynitrate hydrate

Zirconium tert-butoxide

Zirconium acetylacetonate

## 1. Introduction

For decades, conversion coatings based on hexavalent chromium ( $\text{Cr}^{6+}$ ) were used to protect steel from corrosion in infrastructure, manufacturing, and transportation. However,  $\text{Cr}^{6+}$  is carcinogenic, leading to numerous restrictions being put in place since the 1980s. Since then, the automotive and aerospace industries have migrated to zinc phosphate-based systems. These systems tend to be porous which can negatively affect the corrosion mitigation performance. To remedy this, a chromatic sealing step is used to further improve its barrier properties, but increases the environmental and health hazards in the process [1,2]. More recently, zirconium oxide-based pretreatments have become more appealing as they have shown to reduce the environmental impact while providing corrosion performance similar to phosphate-based coatings on certain substrates. However, these are immersion-based processes that require the treatment of large amounts of hazardous waste, large costs associated to protect staff, and large amounts of energy needed to heat and continuously stir the precursor baths [2,3].

Plasma-based processes can serve as a wet chemical waste-free surface modification alternative to the current state-of-the-art. Low pressure plasma systems have long been used to deposit materials for a broad

range of applications [4–7]. In fact, low temperature plasma assisted chemical vapor deposition (PECVD) and atomic layer deposition of zirconium oxide is a well-studied process for the deposition of dielectrics in semiconductor applications [8,9]. However, these processes require low-pressure environments which make them unsuitable for large area applications. Recent advancements in atmospheric pressure plasma (APP) technology have made it possible to modify surfaces without the need for any vacuum components. These systems have also shown that they can clean heavily contaminated surfaces and increase their wettability [10]. Furthermore, many studies have demonstrated that APP processes can be used to deposit high quality coatings allowing for surface cleaning and deposition to be conducted using the same source [11–17].

Atmospheric pressure PECVD is perhaps the most commonly used method to deposit coatings as this process can draw upon a library of precursors typically used in low pressure applications. While a large variety of zirconium precursors are available to be used, not all are feasible due to some combination of toxicity, lack of stability (i.e. moisture and light sensitivity), low volatility, and high costs. For example, zirconium amide precursors, such as tetrakis(ethylmethylamido)zirconium, have good vapor pressure but are toxic, hard to handle and tend to be expensive making them unsuitable for the

\* Corresponding author.

E-mail address: [druzic@illinois.edu](mailto:druzic@illinois.edu) (D.N. Ruzic).

<https://doi.org/10.1016/j.tsf.2021.138815>

Received 30 November 2020; Received in revised form 29 June 2021; Accepted 29 June 2021

Available online 6 July 2021

0040-6090/© 2021 Elsevier B.V. All rights reserved.

intended application. In this study, zirconium tert-butoxide (ZTB) and zirconium acetylacetonate ( $Zr(acac)_4$ ) were selected as zirconium precursors that met the majority of the application requirements. Like other metal alkoxides, ZTB is prone to hydrolysis, but it was tested none the less as it has good vapor pressure at room temperature [18].  $Zr(acac)_4$ , on the other hand, is far more stable compared to ZTB, but it has a low sublimation pressure at room temperature [19,20]. While both of these have been used to deposit coatings in low pressure systems, their feasibility to deposit a coating in an open atmosphere plasma system remains untested [21,22].

Due to limitations specific to organometallic precursors, other deposition processes and precursors were explored. Recent, advancements in liquid assisted plasma enhanced CVD (LA-PECVD) have demonstrated the effectiveness of using metal salts to produce inorganic thin films [11–14,17,23]. This process shows great promise as a high vapor pressure precursor is not required. Instead, precursors can be dissolved in solvents such as water, sprayed on to surfaces and then treated with plasma to deposit a coating. While LA-PECVD has shown great potential, its feasibility to deposit zirconium oxide has not been demonstrated. Hence, LA-PECVD with zirconium oxynitrate ( $ZrO(NO_3)_2$ ) is also put to test in this work. This work aims to demonstrate the feasibility of depositing coatings using these precursors and compare the morphology and the composition of the coatings deposited.

## 2. Experiment setup

### 2.1. Atmospheric pressure plasma source

A schematic of the plasma source setup can be found in Fig. 1. The atmospheric pressure plasma jet (APPJ) consists of two concentric electrodes allowing for the microwaves to propagate in between the annulus cavity. A titanium (OD 0.25 inch) tube is used as the inner electrode. The remainder of the APPJ, including the outer electrode (ID 0.625 inch) is made up of copper. The microwaves enter this cavity through a 7/16 DIN connector mounted on the side of the torch. The position of the back-wall and the inner electrode can be adjusted to tune the APPJ. This torch houses its own modular gas curtain and converging nozzle. The modular gas curtain can be used to mitigate any contamination from the surrounding environment. The converging nozzle, on the other hand, can be used to focus the plasma to allow accessing narrow trenches. A more detailed description of the APPJ can be found

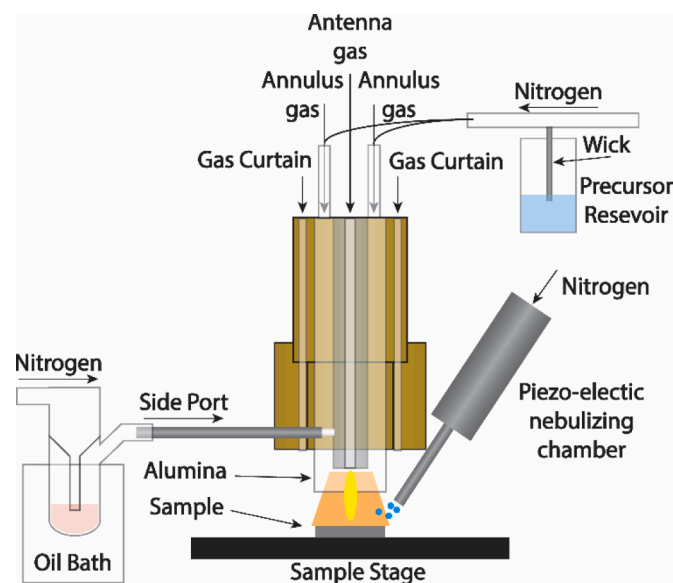


Fig. 1. A schematic of the setup used for all the processes described in this work.

elsewhere [24].

A 6kW power supply (Cober S6F) is used to excite 2.45 GHz microwaves. A series of waveguides are used to deliver these microwaves to the APPJ. A water-cooled circulator was used to negate any damage to the power supply due to reflected waves. Microwave power meters and stub tuners, both in series with waveguides, were used to always keep the reflected power below 5% during the experiments.

The APPJ source can sustain a plasma using helium, argon, nitrogen, oxygen, or any combination of these gases. The gas flowrates were controlled using a set of flow regulators or mass flowmeter. The operating gases were injected through the annulus region of the torch. The plasma is struck with 10–20 LPM of helium with approximately 400 W after which the gas composition can be switched with any of gases listed. A minimum of 500 W was required for a steady discharge of a nitrogen-argon plasma. The setup allows for the precursor to be injected through multiple feeds. The cavity within the inner electrode can also act as a separate inlet for the gasses and precursors. Precursors with low sublimation pressure, which typically require heating, can be fed through the side of the applicator. This setup also features an aerosolizer which can allow for various liquid solutions to be sprayed directly onto the sample to be treated immediately by the plasma.

### 2.2. Deposition process

Single crystal undoped silicon wafers and commercially available mirror polished Al 6061 extrusions (1.5 mm) were cut into 15 x 15 mm coupons for use as substrates. The aluminum substrates had an average surface roughness of approximately 50 nm as measured by a contact profilometer. Prior to deposition, the substrates were chemically cleaned using isopropyl alcohol and allowed to dry. For the samples deposited using the LA-PECVD process, additional cleaning was performed using a single plasma pass to allow for the dispersed droplets to properly wet the surface. While no separate plasma precleaning was conducted during the deposition with ZTB and  $Zr(acac)_4$ , the leading edge of the plasma volume is expected to provide some cleaning prior to the deposition [10]. This was further verified by conducting contact angle measurements which indicated a reduction of contact angle from  $48^\circ$ – $19^\circ$  after a single cleaning step on an as received aluminum sample. The temperature of the substrates was obtained using a thermocouple inserted into a small hole drilled on side of the samples.

For ZTB and  $Zr(acac)_4$ , a bubbler type delivery was used to transport the precursor vapors to the plasma. For ZTB, 5 mL of precursor was loaded in the bubbler and these vapors were fed directly through the inner electrode. A heated setup was needed for  $Zr(acac)_4$  since the sublimation pressure is negligible at room temperature. Approximately 3 grams of precursor was loaded in a glass bubbler submerged in heated mineral oil bath. Throughout the experiment, the oil temperature was maintained between  $172$ – $186^\circ\text{C}$  in order to melt the  $Zr(acac)_4$  powder. Once the precursor was melted, nitrogen was passed through the bubbler to carry the precursor to the APPJ. The carrier gas was also heated to this temperature using heat wire wrapped around the gas tubing. However, it was not possible to transport the heated gases through the inner electrode without the precursor vapor condensing on the surfaces due to the rapid heat loss to the inner electrode walls. Instead, the precursor vapor was directly injected through a small hole 12 mm from the edge of the outer cathode. A schematic of the setup can be found in Fig. 1. For both processes, the sample passed underneath the plasma at a velocity of 4 mm/s.

Typical of metal salts,  $ZrO(NO_3)_2$  has negligible sublimation pressure even at modestly elevated temperatures.  $ZrO(NO_3)_2$  has been shown to undergo decomposition as low as  $191.85 \pm 50^\circ\text{C}$  [25]. As a result, traditional vapor phase PECVD was not possible. For this reason, a different strategy was adopted where the precursor was applied directly on to the substrate and then plasma treated [11–14,17]. To do so,  $ZrO(NO_3)_2$  was dissolved (0.5 M in distilled water) and the solution was wicked onto a 16 kHz piezoelectric nebulizer to generate a stream of

dispersed droplets within a closed container. A carrier gas through this chamber was used to carry these dispersed droplets directly on the substrate. Finally, the solution was converted to zirconium oxide by treating it with an atmospheric pressure plasma.

Due to the nature of the atmospheric plasma source in use, stable operating regimes varied significantly for each precursor delivery method with regard to power, gas composition and flow rates. A summary of empirically determined ranges of stable operating conditions for each process can be found in Table I: Range of parameters tested for each precursor is shown. All substrates were placed 10 mm below the plasma source with the exception of  $Zr(acac)_4$  where the stage height was set to 15 mm. While critical for description of the experiments performed, the table cannot be used to represent a design of experiments, or be used for direct comparison between precursors or delivery methods because of source stability.

### 2.3. Characterization of coatings

The surface morphology, and in some cases, cross-sections of a cleaved coating deposited on silicon wafers, were imaged using scanning electron microscope (SEM) (Hitachi 4800) with a through-the lens detector. The SEM operating voltage was set to 10 kV. Prior to imaging, the samples were sputter coated with 10–15 nm of Au-Pd to minimize charging. Cross-section imaging on aluminum samples were conducted by ion milling a 6  $\mu\text{m}$  deep trench using a focused ion beam (FIB) of gallium ions (30 kV with currents ranging from 80 pA–7 nA) and then imaged using SEM (PHI Helios) at an operating voltage of 5 kV. A 1.5  $\mu\text{m}$  thick layer of Pt was deposited atop the surface before the trench was milled to protect the underlying surface from damage induced by FIB.

X-ray photoelectron spectroscopy (XPS) (Kratos Axis ULTRA) was used for the surface composition characterization of the coatings. This instrument features a monochromatic Al  $K\alpha$  X-Ray source. To mitigate surface charging, the samples were mounted on an ungrounded stage and were exposed to a constant electron flux as the spectra was collected. Depth profile XPS was conducted at a laboratory built XPS facility at the University of Illinois. This instrument is capable of conducting XPS analysis using Al  $K\alpha$  X-Ray source along with Specs PHOIBOS 150 hemispherical energy analyzer. It also has the ability to sputter etch coatings with an argon ion source. For the depth profile analysis reported in this work, argon ion beam with ion energies of 500 eV and 5 keV was used with an ion current of 37  $\mu\text{A}/\text{cm}^2$ . The XPS data collected was analyzed using CasaXPS.

## 3. Results

### 3.1. Zirconium tetra-tert butoxide (ZTB)

Deposition from ZTB was conducted on silicon substrates using the conditions listed in Table I: Range of parameters tested for each precursor is shown. All substrates were placed 10 mm below the plasma source with the exception of  $Zr(acac)_4$  where the stage height was set to 15 mm. Substrate temperatures for aluminum coupons were determined inserting shielded K type thermocouples into a blind hole milled into the side of coupons. Measured temperatures consistently dwelt close to 200 °C. Equivalent temperatures for silicon coupons could not

be measured but are expected to be similar. After processing, the surface showed presence of a coating, however, the deposited material could be removed upon light rubbing with a gloved finger or a delicate task wipe (Kimwipe), indicating very poor adhesion of the material to the substrate. A closer inspection under SEM revealed a surface covered with clustered nanoparticles (Fig. 2a). This observation was consistent for all the carrier gas flow rates tested (0.1–1 LPM). A control experiment was conducted in the absence of plasma and the cross-section SEM showed particles of similar features on the surface (Fig. 2b).

### 3.2. Zirconium acetylacetonate ( $Zr(acac)_4$ )

Zirconia films were also deposited from  $Zr(acac)_4$  at a variety of powers and gas flowrates (Table I: Range of parameters tested for each precursor is shown. All substrates were placed 10 mm below the plasma source with the exception of  $Zr(acac)_4$  where the stage height was set to 15 mm.) with most consistent results achieved at 600 W, 20 LPM of air with 1 LPM  $N_2$  as a carrier gas. A typical substrate temperature of 260 °C was recorded for these conditions. These conditions resulted in a coating with a deposition width greater than the width of the substrate (15 mm). The surface and the cross-section micrographs were obtained using SEM and FIB, respectively (Fig. 3) and were taken from the center of the deposition path. These micrographs showed an evenly coated aluminum surface. The absence of cracks, pits or any other defects was also encouraging. A coating of approximately 100 nm was measured on the cross-section SEM.

Depth profile XPS was then used to determine the composition through the thickness of the coating. High resolution spectrums of O 1s, C 1s, Zr 3d and Al 2p were obtained at various depths. The concentration profiles were calculated and then plotted as a function of depth and can be found in Fig. 4. While the surface was heavily contaminated with carbon, a Zr:O:C ratio of 1:2.0:0.6 was measured at a depth of approximately 0.25  $\mu\text{m}$ , which corresponded to the depth that had the highest zirconium concentration.

### 3.3. Zirconium oxynitrate hydrate ( $ZrO(NO_3)_2$ )

For the third process,  $ZrO(NO_3)_2$  droplets were transported to the aluminum substrate at a rate of approximately 13 mg/min immediately prior to plasma treatment. After deposition, it was noted that almost all of the coating was deposited in a narrow band approximately 5 mm wide with the thickest regions in the center of the band.

Surface micrographs, Fig. 5, revealed that the coatings had an atypical overlapping circle morphology. These features had diameters between 15–30  $\mu\text{m}$ . Several cracks and other defects were also observed on the surface of the coatings. Fig. 5b shows a cross-section micrograph of the coating obtained after milling the surface using FIB. An average coating thickness of 518 nm was measured over three different locations on the coating. Both the surface and cross-section micrographs showed the presence of numerous cracks which propagated through the entire cross-section of the coating.

The surface composition of the coatings was characterized using XPS, with a particular emphasis on determining whether there was significant nitrate, hydrate, or hydroxyl concentrations in the films. After identifying the major peaks in the survey spectrum, high resolution spectrums

**Table I**

Range of parameters tested for each precursor is shown. All substrates were placed 10 mm below the plasma source with the exception of  $Zr(acac)_4$  where the stage height was set to 15 mm.

Name of the precursor	Feed channel	Plasma power [W]	Gas composition	Flowrate [LPM]	Carrier gas Flowrate [LPM]	Stage velocity [mm/s]	# of cycles
Zirconium tetra-tert butoxide, ZTB	Antenna	600	Argon   Nitrogen	17   4	0.1–1	4	10
Zirconium acetylacetonate, $Zr(acac)_4$	Side	600–800	Air	20	0.5–1.5	4	10 - 40
Zirconium oxynitrate hydrate, $ZrO(NO_3)_2$	Aerosolized	600	Argon   Nitrogen	17   4	0.8	4–36	2 - 10

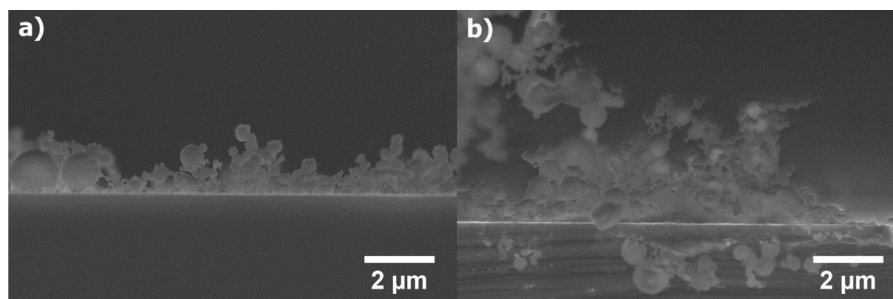


Fig. 2. Clustered nanoparticles on silicon substrates synthesized using ZTB and deposited a) with and b) without the plasma. In each case, the carrier gas flow rate was set to 1 LPM. Very little difference was observed in the morphology of the nanoparticles produced with and without plasma.

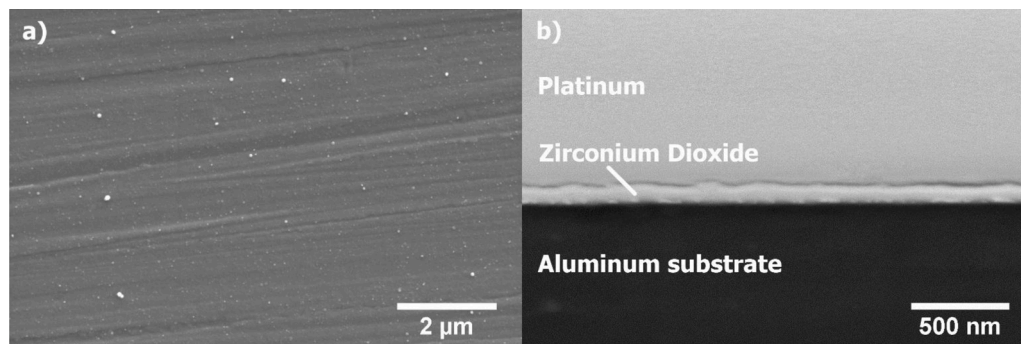


Fig. 3. a) Surface and b) cross-section SEM micrographs of the coating deposited using  $Zr(acac)_4$ . The coating was deposited using 600 W plasma sustained using 20 LPM air and a carrier gas flow rate of 1.5 LPM  $N_2$ . The thickness of the coating was approximately 115 nm.

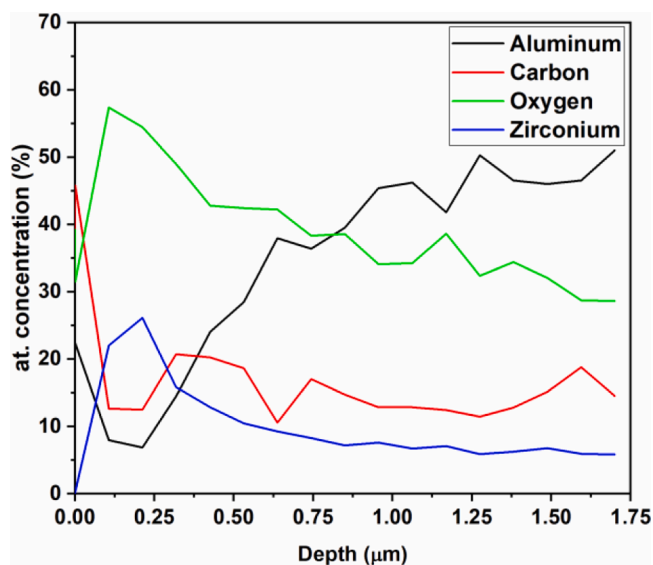


Fig. 4. Composition of the coating deposited using zirconium acetylacetonate as a function of depth obtained using XPS.

of O 1s, N 1s, C 1s and Zr 3d peaks were obtained (Fig. 6). To estimate the concentration of  $H_2O$  and  $-OH$  species, area constraints were imposed for all other components in O 1s core level (Table II). These constraints allow for the estimation of the total contribution to the O 1s peak from carbon contaminants, zirconium dioxide and nitrates identified in the C 1s, Zr 3d and N 1s peaks, respectively. The remainder of the O 1s peak is comprised of contributions from  $OH^-$  and  $H_2O$ . Since the separation between  $OH^-$  and  $H_2O$  peaks is large enough, the concentration of each can be calculated. The area constraints were determined by using a scaling factor which accounts for the relative sensitivity factor

(R.S.F) and the stoichiometric ratio of oxygen atoms to that of Zr, N and C for these components. An example calculation of the area constraint for  $O=C-O$  can be seen in the equation below.

$$Area(O=C-O)_{O\ 1s} = Area(O=C-O)_{C\ 1s} \left( \frac{n_O}{n_C} \right) \left( \frac{R.S.F\ O\ 1s}{R.S.F\ C\ 1s} \right)$$

Here,  $n$  is the number of atoms of each species in a particular component. The values for R.S.F were provided by the manufacturer (Kratos Analytical). A summary of all the peaks identified along with peak position, FWHM and area constraints used can be found in Table II.

An example of the measured spectrum, along with the fits, can be found in Fig. 6. The fitting procedure was repeated for several samples, each deposited using different stage velocity (different plasma exposure times). The concentration of all oxygen containing species were then studied as a function of stage velocity (Fig. 7a). The results showed that as the sample velocity is increased, the zirconium-bound oxygen concentration at the surface decreases significantly while the surface nitrate-bound oxygen concentration increases. The other components did not show any change as a function of the exposure time. All of the carbon peaks observed are likely artifacts of environmental contamination post deposition since there was no carbon in the precursor chemicals. Very little water was present in any of these samples, which implied that the solvent was almost completely volatilized for each case. Likewise, the hydroxyl molecules did not show any significant change with exposure time either. The substrate temperature during the deposition was not constant due to the motion of the stage. The mean peak substrate temperatures were obtained by taking the average of the peak temperature after every cycle. This plot can be found in Fig. 7b along with the average substrate temperature. It was interesting to note that a higher peak temperature was observed for the sample deposited at 8 mm/s than the one deposited at 4 mm/s. While the exact reason for this is unknown, it is speculated that arcing during the deposition may have driven the temperature higher.

Depth profile XPS was used to determine the bulk composition of the

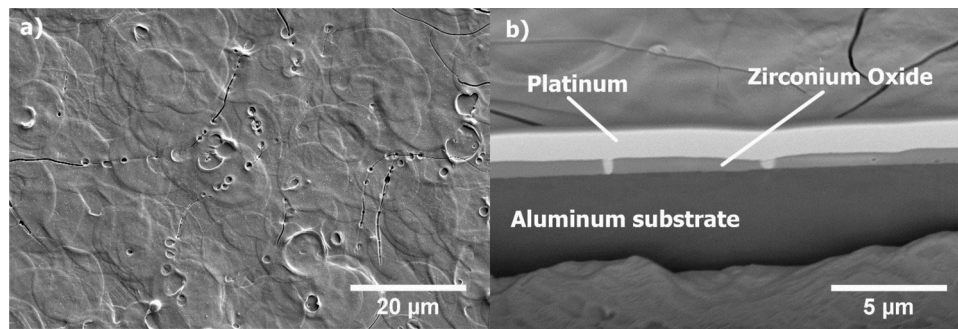


Fig. 5. Micrographs of the a) coating surface and b) cross-section of the coatings deposited using zirconium oxynitrate hydrate.

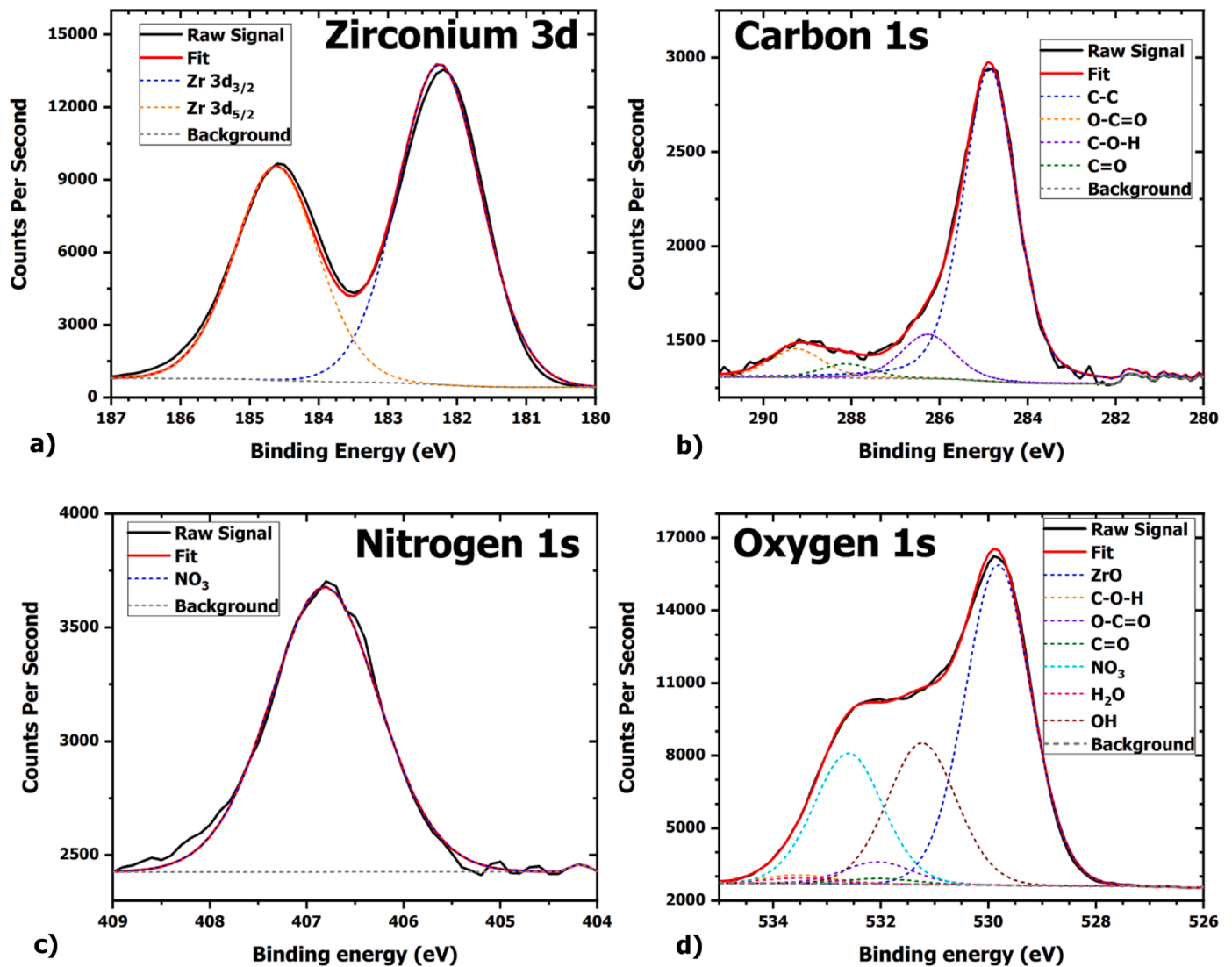


Fig. 6. High resolution surface XPS spectrum of a) Zr 3d, b) C 1s, c) N 1s and d) O 1s peaks. The sample was fabricated at a velocity of 4 mm/s. Component peak fitting was performed using the constraints described in Table II.

sample fabricated with the stage velocity of 4 mm/s. The relative concentration of the O 1s, C 1s, N 1s and Zr 3d peaks were plotted as a function of approximate depth (Fig. 8). The results showed that both the nitrogen and the carbon were only present on the surface. Within the bulk, a Zr:O ratio of 1:2.2 was measured at an approximate depth of 4 nm.

#### 4. Discussion

Out of the three different precursors discussed in this work, only two were feasible for deposition of zirconia coatings. While the vapor pressure of ZTB is significantly higher than the other two, its susceptibility to hydrolysis makes it extremely difficult to work with especially in an open atmosphere system. By comparing the micrographs shown in

Table II

Description of various peaks used for fitting XPS spectrums is shown here. The table also contains various constraints used during the fitting process [26–28]. R.S.F values provided by the manufacturer (Kratos Analytical).

		Peak ID	R.S.F	Position Constraints (eV)	FWHM Constraint (eV)	Area Constraint
Zirconium-3d	ZrO <sub>2</sub>	A	2.576	181.2–183.1	1.0–2.0	-
	ZrO <sub>2</sub>	B		183.6–185.6	A * 1	A * 0.67
Carbon-1s	C-C	C	0.278	284.3–285.2	1.4	-
	C-O-H	D		285.5–286.5	C * 1	-
	O-C=O	E		288.6–289.6	C * 1	-
	C=O	F		287.3–288.5	C * 1	-
		G		405.9–407.9	1.4	-
Nitrogen-1s	NO <sub>3</sub>	H	0.780	529.7–531.1	1.0–2.0	A * 1.01
Oxygen-1s	ZrO <sub>2</sub>	I		531.6–533.6	1.0–2.0	G * 4.90
	C-O-H	J	532.6–533.8	I * 1	D * 2.80	
	O-C=O	K	532.0–532.4	I * 1	B * 5.61	
	C=O	L	532.0–533.6	I * 1	F * 2.80	
	OH	M	530.0–532.0	1.0–2.0	-	
	H <sub>2</sub> O	N	531.9–533.5	1.0–2.0	-	

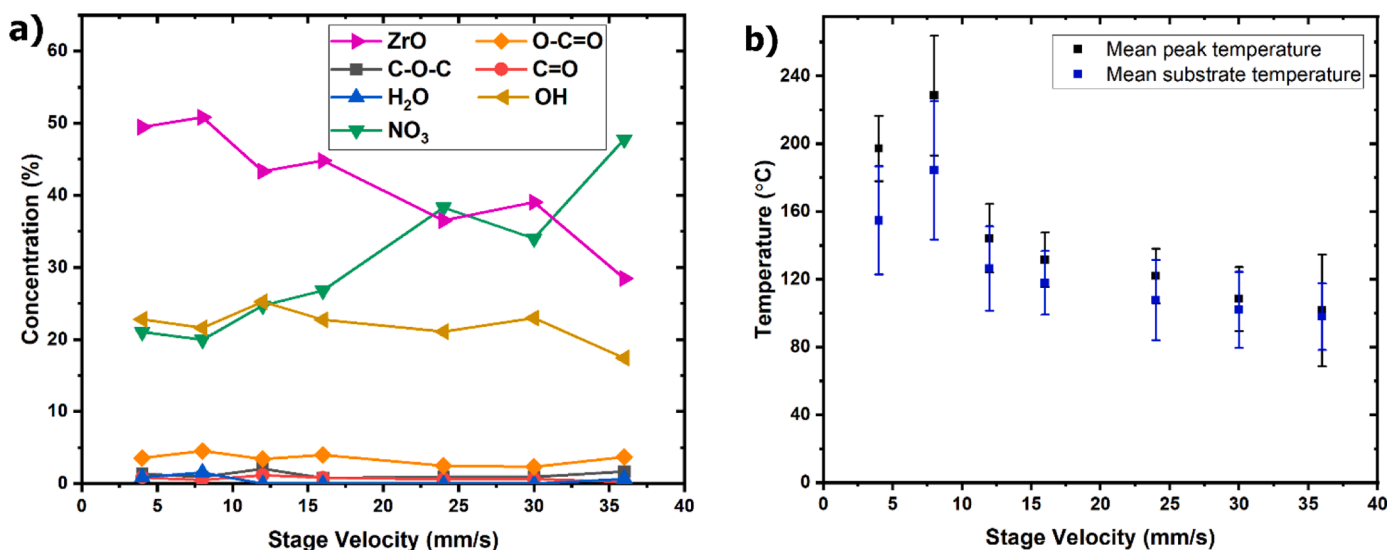


Fig. 7. a) Change in the surface composition of the oxygen containing species were collected as a function of the stage velocity. The composition data was collected by peak fitting oxygen high resolution XPS spectrum. b) The average of the peak temperatures measured during the deposition of these samples are reported as a function of the stage velocity.

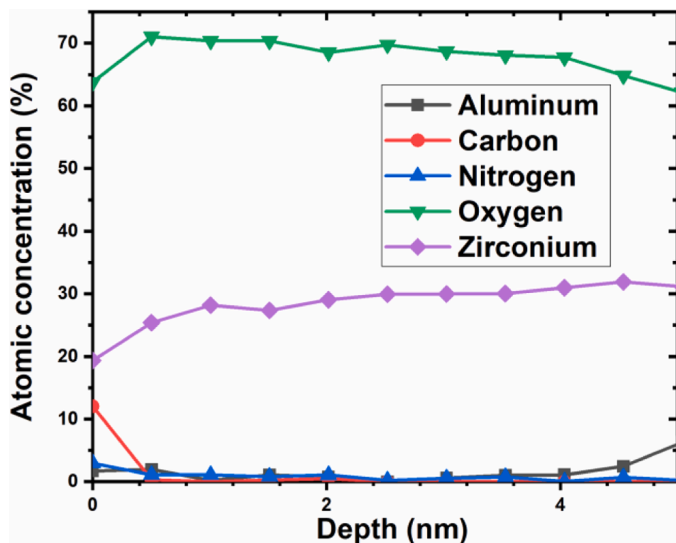


Fig. 8. Change in the coating composition as a function of depth for the coating deposited using ZrO(NO<sub>3</sub>)<sub>2</sub> at a stage velocity of 4 mm/s.

Fig. 2, it is very apparent that synthesis of these particles was likely occurring during transport to the plasma. It is presumed that the precursor undergoes premature decomposition by hydrolysis followed by agglomeration of reaction products. This observation was consistent for all the experiments conducted using this precursor, despite careful attempts to remove moisture from the transport lines. In a previous study, Bradley et al. noted that the hydrolysis of ZTB can be easily initiated by water desorbed from surfaces [29]. To completely mitigate this issue, a careful bakeout of the apparatus and all gas lines, both upstream and downstream, would be required to remove any adsorbed water from the surfaces. Premature decomposition not only results in poor adhesion, but it also precursor depletion which can reduce the growth rate of the coating.

Unlike ZTB, Zr(acac)<sub>4</sub> is far more chemically stable in open atmosphere. The results in Fig. 2 show that this process is capable of depositing zirconium oxide coatings. Carbon contamination in coatings deposited with β-diketonate compounds is a common issue [30]. To mitigate this, an air plasma was used to oxidize excessive carbon content instead of the traditional approach of heating the samples. Despite these efforts, the XPS composition profile in Fig. 4 showed that there was significant carbon contamination on the surface, and some incorporated within the bulk. Further investigation with a higher oxygen content within the plasma could be performed to determine whether the carbon

content could be reduced in the coatings.

A bigger issue with this process was the need to heat the precursor to attain a sufficiently high vapor pressure. During the experiments, it was noted that the precursor underwent chemical degradation as it was heated to its melting point. TGA analysis of  $Zr(acac)_4$  revealed a weight loss process maximizing at 181 °C, right at the operating temperatures of 172–186 °C. A weight loss of 17.4% was measured as the temperature was increased up to 181 °C. A similar observation was made by Ismail who identified that the weight loss taking place between 150–200 °C can be attributed to the release of  $C_3H_4$  [31]. While the decomposition does not directly impede the ability to deposit zirconium oxide coatings, it does hamper its scalability. It was not feasible to re-melt a batch of decomposed precursor once it solidified. This is likely due to the cross-linking of the molecules of the decomposed byproducts as it cools down. This wastage makes this process less appealing from a financial standpoint.

The premature decomposition of the precursor is not an issue in the LA-PECVD process, as all of the reactions take place on the surface of the substrate. Unlike  $Zr(acac)_4$ , no additional heating elements are required to increase the volatilization. The mass transport of the precursor is a function of the dissolved salt concentration and carrier gas flow rate, and is not dependent on the vapor pressure. Ideally, the droplets would be injected directly into the plasma to take advantage of gas phase reactions of a PECVD process. Previous studies conducted with a dielectric barrier discharge have shown to reduce the overall diameter of the injected aerosols. This occurs due to charging of the droplets in the plasma, which can lead to deformation and splitting of larger droplets [32,33]. It was speculated that division of micron-sized droplets injected into the plasma would result in near vapor-like dispersion of precursor in the gas phase. However, an attempt at doing so resulted in the formation of nanoparticles rather than a coating. The high temperature of the plasma environment, which is much greater than the evaporation temperature of the solvent, can lead to rapid volatilization of the solvent and partial precipitation of the salt in flight. Next, the decomposition of the salt precursor is initiated and is followed by nucleation of grains and larger particles formed predominately of the final oxide. This process is of interest to many and have been studied by several groups [34–36]. Therefore, spraying the salts directly into the plasma is not suitable for deposition of coatings in plasmas operating with high gas temperatures. By spraying the salt solution directly onto the surface before plasma treatment, the deposition rate is limited by the decomposition rate of the precursor under the plasma allowing for higher deposition rates compared to vapor delivery. A deposition rate of 40 nm/s was achieved using this process as opposed to 0.7 nm/s corresponding to the best result using  $Zr(acac)_4$ .

The decomposition of the precursor on the surfaces can be attributed to a combination of thermal effects and plasma based reactions. From the data presented in Fig. 7b, it was observed that the mean surface temperatures were greater than 100 °C for all of the tested stage velocities, however, the maximum surface temperature was below the  $ZrO(NO_3)_2$  decomposition temperature ( $191.85 \pm 50$  °C [25]) for all stage velocities above 8 mm/s. While water could evaporate solely through thermal processes, it is unlikely that all the zirconium dioxide formation is due to thermal processes. The surface composition differences observed in Fig. 7b also further indicated that the decomposition was not purely thermal. The samples that had increased residence time in the plasma (lower velocities) showed a more efficient breakdown of the precursor, as evidenced by lower nitrate concentrations at the coating surface, even though the maximum temperature was roughly equivalent for all velocities above 8 mm/s. Reactive species in the plasma, such as hydroxyl and oxygen radicals along with energetic electrons, likely play a significant role in altering the surface composition, facilitating the breakdown of the zirconium salts [23]. The role of these reactive species in the decomposition of the salts is likely pronounced at the surface since the radical species penetration depth is less than the film thickness from a single application pass. Sub-surface nitrate decomposition must rely on

a mixture of thermal decomposition and diffusion. The lack of contaminants in the bulk, as evidenced by Fig. 8, along with low nitrogen and expected carbon at the surface indicates that it is likely that the coating composition continues to evolve with subsequent plasma treatments. Taken together, the coating data indicates that both thermal and plasma-based decomposition play a significant role in the coating synthesis.

While the bulk composition was close to that of the theoretical composition of zirconia, micrographs shown in Fig. 5 revealed numerous cracks and pin holes in the coatings. The pin holes in the coatings are likely the result of occasional arcing during deposition [37]. The lack of uniformity in the coatings can hinder its ability to provide sufficient corrosion protection as seen for other coating systems [38]. Optimization of the morphology of this coating will be further investigated in the near future.

## 5. Conclusions

The feasibility of depositing zirconium oxide using an open atmosphere plasma source was tested using ZTB,  $Zr(acac)_4$  and  $ZrO(NO_3)_2$  as precursors. These precursors were selected for their relatively low toxicity allowing for ease of handling when operating in an open atmosphere system. It was shown that it was possible to deposit coatings using  $Zr(acac)_4$  and  $ZrO(NO_3)_2$ . However, decomposition of the ZTB in the gas lines due to hydrolysis resulted in the synthesis of nano-spheres during transport, rather than the deposition of a coating. The process involving  $Zr(acac)_4$ , on the other hand, resulted in a 100 nm thin coating with minimal defects observed under SEM. XPS results indicated a bulk Zr:O:C concentration of 1:2.0:0.6. In addition to this, an emerging method of LA-PECVD was used to deposit zirconia coatings using  $ZrO(NO_3)_2$ . This process shows promise as high deposition rates can be achieved very easily with minimal contamination. In addition, the delivery of the precursor used in this process mitigates any gas phase reactions which can lead to undesired formation and deposition of particles. Furthermore, this process does not require any additional heating elements as the mass transport of the precursor is independent of its sublimation pressure. The depth profile XPS results of the coatings deposited using this process showed a bulk Zr:O composition of 1:2.2 was obtained, with little to no nitrogen or carbon present in the coatings. While the surface micrographs indicated numerous cracks in these coatings, the ease of processing, good deposition rate and lack of chemical contaminants showed that the LA-PECVD of  $ZrO(NO_3)_2$  is a promising method for the deposition of zirconium oxide coatings and merits further studies to optimize the process.

Dhruval Patel: Data Curation, Methodology, Writing

Lucia Bonova: Methodology, Supervision,

Zachary Jeckell: Data Curation

David Eitan Barlaz: Methodology, Supervision, Writing - Review & Editing,

Santanu Chaudhuri: Funding acquisition

Daniel Krogstad: Methodology, Funding acquisition, Supervision, Formal analysis

David Ruzic: Funding acquisition, Writing - Review & Editing

## Declaration of Competing Interest

The authors declare that they have no known competing financial interests or personal relationships that could have appeared to influence the work reported in this paper.

The authors declare the following financial interests/personal relationships which may be considered as potential competing interests:

## Acknowledgements

The authors would like to thank Dr. Rick Haasch and Eric Lang for their help with XPS data collection and interpretation. The authors

would also like to thank Arash Samaei, Professor Jessica Krogstad, Dr. Joseph Osborne and Dr. Brian Jurczyk for providing various suggestions through the course of this work. This work was supported by the Strategic Environmental Research and Development Program under Project No. WP-2742. SEM, FIB and XPS were carried out in the Materials Research Laboratory Central Research Facilities.

## References

- [1] T.S.N.S. Narayanan, Surface pretreatment by phosphate conversion coatings - a review, *Rev. Adv. Mater. Sci.* 9 (2005) 130–177.
- [2] I. Milošev, G.S. Frankel, Review—conversion coatings based on zirconium and/or titanium, *J. Electrochem. Soc.* 165 (2018) C127–C144, <https://doi.org/10.1149/2.0371803jes>.
- [3] P. Puomi, H.M. Fagerholm, J.B. Rosenholm, K. Jyrka, Comparison of different commercial pretreatment methods for hot-dip galvanized and Galvan coated steel, *Surf. Coatings Technol.* 115 (1999) 70–78, <http://www.sciencedirect.com/science/article/pii/S025789729900170X>.
- [4] R.F. Bunshah, C.V. Deshpandey, Plasma assisted physical vapor deposition processes: a review, *J. Vac. Sci. Technol. A Vacuum, Surfaces, Film.* 3 (1985) 553–560, <https://doi.org/10.1116/1.572993>.
- [5] L. Martinu, D. Poitras, Plasma deposition of optical films and coatings: a review, *J. Vac. Sci. Technol. A Vacuum, Surfaces, Film.* 18 (2000) 2619–2645, <https://doi.org/10.1116/1.1314395>.
- [6] E. Kessels, S. Heil, E. Langereis, H. van Hemmen, H. Knoops, W. Keuning, R. van de Sanden, Opportunities for plasma-assisted atomic layer deposition, *ECS Trans* (2007) 183–190, <https://doi.org/10.1149/1.2721487>.
- [7] C. Deshpandey, R.F. Bunshah, Plasma assisted deposition techniques and synthesis of novel materials, *Thin Solid Films* 163 (1988) 131–147.
- [8] E.T. Kim, S.G. Yoon, Characterization of zirconium dioxide film formed by plasma enhanced metal-organic chemical vapor deposition, *Thin Solid Films* 227 (1993) 7–12, [https://doi.org/10.1016/0040-6090\(93\)90179-5](https://doi.org/10.1016/0040-6090(93)90179-5).
- [9] J. Koo, Y. Kim, H. Jeon, ZrO<sub>2</sub> gate dielectric deposited by plasma-enhanced atomic layer deposition method, *Japanese J. Appl. Physics, Part 1 Regul. Pap. Short Notes Rev. Pap.* 41 (2002) 3043–3046, <https://doi.org/10.1143/JJAP.41.3043>.
- [10] L. Bónová, W. Zhu, D.K. Patel, D.V. Krogstad, D.N. Ruzic, Atmospheric pressure microwave plasma for aluminum surface cleaning, *J. Vac. Sci. Technol. A* 38 (2020), 023002, <https://doi.org/10.1116/1.5132912>.
- [11] Y. Sui, Y. Dai, C.C. Liu, R.M. Sankaran, C.A. Zorman, A new class of low-temperature plasma-activated, inorganic salt-based particle-free inks for inkjet printing metals, *Adv. Mater. Technol.* 4 (2019) 1–10, <https://doi.org/10.1002/admt.201900119>.
- [12] T. Liu, K. Premasiri, Y. Sui, X. Zhan, H.A.B. Mustafa, O. Akkus, C.A. Zorman, X.P. A. Gao, R.M. Sankaran, Direct, transfer-free growth of large-area hexagonal boron nitride films by plasma-enhanced chemical film conversion (PECFC) of printable, solution-processed ammonia borane, *ACS Appl. Mater. Interfaces.* 10 (2018) 43936–43945, <https://doi.org/10.1021/acami.8b17152>.
- [13] T. Liu, X. Liu, S. Bhattacharya, Z. Ye, R. He, X.P.A. Gao, R. Akolkar, R.M. Sankaran, Plasma-induced fabrication and straining of MoS<sub>2</sub> films for the hydrogen evolution reaction, *ACS Appl. Energy Mater.* 2 (2019) 5162–5170, <https://doi.org/10.1021/acsaem.9b00843>.
- [14] R. Mauchauffé, S. Kang, S.Y. Moon, Fast formation of amorphous titanium dioxide thin films using a liquid-assisted plasma-enhanced deposition process in open air, *Surf. Coatings Technol.* 376 (2019) 84–89, <https://doi.org/10.1016/j.surfcoat.2018.01.088>.
- [15] M.A. Mione, I. Katsouras, Y. Creghton, W. van Boekel, J. Maas, G. Gelinck, F. Roozeboom, A. Illiberi, Atmospheric pressure plasma enhanced spatial ALD of ZrO<sub>2</sub> for low-temperature, large-area applications, *ECS J. Solid State Sci. Technol.* 6 (2017) N243–N249, <https://doi.org/10.1149/2.0381712jss>.
- [16] D. Merche, N. Vandencastele, F. Reniers, Atmospheric plasmas for thin film deposition: a critical review, *Thin Solid Films* 520 (2012) 4219–4236, <https://doi.org/10.1016/j.tsf.2012.01.026>.
- [17] J. Schäfer, K. Fricke, F. Mika, Z. Pokorná, L. Zajíčková, R. Foest, Liquid assisted plasma enhanced chemical vapour deposition with a non-thermal plasma jet at atmospheric pressure, *Thin Solid Films* 630 (2017) 71–78, <https://doi.org/10.1016/j.tsf.2016.09.022>.
- [18] B.D.C. Bradley, J.D. Swanwick, Vapour pressures of metal alkoxides. Part I. Titanium tetra-tert.-butoxide and -amlyoxide, *J. Chem. Soc.* (1958) 3207–3214, <https://doi.org/10.1039/JR9580003207>.
- [19] N.B. Morozova, S.V. Sysoev, I.K. Igumenov, A.N. Golubenko, Study of temperature dependence of saturated vapour pressure of zirconium(IV) β-diketonates, *J. Therm. Anal.* 46 (1996) 1367–1373, <https://doi.org/10.1007/BF01979249>.
- [20] M. Balog, M. Schieber, M. Michman, S. Patai, The chemical vapour deposition and characterization of ZrO<sub>2</sub> films from organometallic compounds, *Thin Solid Films* 47 (1977) 109–120, [https://doi.org/10.1016/0040-6090\(77\)90350-9](https://doi.org/10.1016/0040-6090(77)90350-9).
- [21] A.M. Torres-Huerta, M.A. Domínguez-Crespo, E. Ramírez-Meneses, J.R. Vargas-García, MOCVD of zirconium oxide thin films: synthesis and characterization, *Appl. Surf. Sci.* 255 (2009) 4792–4795, <https://doi.org/10.1016/j.apusc.2008.11.059>.
- [22] K. Kukli, M. Ritala, M. Leskelä, Low-temperature deposition of zirconium oxide-based nanocrystalline films by alternate supply of Zr[OC(CH<sub>3</sub>)<sub>3</sub>]<sub>4</sub> and H<sub>2</sub>O, *Chem. Vap. Depos.* 6 (2000) 297–302, [10.1002/1521-3862\(200011\)6:6<297::AID-CVDE297>3.0.CO;2-8](https://doi.org/10.1002/1521-3862(200011)6:6<297::AID-CVDE297>3.0.CO;2-8).
- [23] M. Nikravec, K. Baba, B. Leneindre, F. Rousseau, Role of reactive species in processing materials at laboratory temperature by spray plasma devices, *Chem. Pap.* 66 (2012) 502–510, <https://doi.org/10.2478/s11696-012-0158-y>.
- [24] D.N. Ruzic, Y. Wu, I. Shchelkanov, J. Hong, Z. Ouyang, Apparatus and method for depositing a coating on a substrate at atmospheric pressure, U.S. Patent No. 10167556 (2015).
- [25] S. Yuvaraj, F.Y. Lin, T.H. Chang, C.T. Yeh, Thermal decomposition of metal nitrates in air and hydrogen environments, *J. Phys. Chem. B* 107 (2003) 1044–1047, <https://doi.org/10.1021/jp026961c>.
- [26] G.P. López, D.G. Castner, B.D. Ratner, XPS O 1s binding energies for polymers containing hydroxyl, ether, ketone and ester groups, *Surf. Interface Anal.* 17 (1991) 267–272, <https://doi.org/10.1002/sia.740170508>.
- [27] D. Barreca, G.A. Battiston, R. Gerbasi, E. Tondello, P. Zanella, Zirconium dioxide thin films characterized by XPS, *Surf. Sci. Spectra.* 7 (2000) 303–309, <https://doi.org/10.1116/1.1375573>.
- [28] T.C. Lin, G. Seshadri, J.A. Kelber, A consistent method for quantitative XPS peak analysis of thin oxide films on clean polycrystalline iron surfaces, *Appl. Surf. Sci.* 119 (1997) 83–92, [https://doi.org/10.1016/S0169-4332\(97\)00167-0](https://doi.org/10.1016/S0169-4332(97)00167-0).
- [29] D.C. Bradley, Metal alkoxides as precursors for electronic and ceramic materials, *Chem. Rev.* 89 (1989) 1317–1322, <https://doi.org/10.1021/cr00096a004>.
- [30] A.C. Jones, MOCVD of electroceramic oxides: a precursor manufacturer's perspective, *Chem. Vap. Depos.* 4 (1998) 169–179, [10.1002/\(sici\)1521-3862\(199810\)04:05<169::aid-cvde169>3.3.co;2-y](https://doi.org/10.1002/(sici)1521-3862(199810)04:05<169::aid-cvde169>3.3.co;2-y).
- [31] H.M. Ismail, Characterization of the decomposition products of zirconium acetylacetonate: nitrogen adsorption and spectrothermal investigation, *Powder Technol* 85 (1995) 253–259, [https://doi.org/10.1016/0032-5910\(95\)03025-7](https://doi.org/10.1016/0032-5910(95)03025-7).
- [32] A. Stancampiano, T. Galligani, M. Gherardi, Z. Machala, P. Maguire, V. Colombo, J.M. Pouvesle, E. Robert, Plasma and aerosols: challenges, opportunities and perspectives, *Appl. Sci.* 9 (2019), <https://doi.org/10.3390/app9183861>.
- [33] P.D. Maguire, C.M.O. Mahony, C.P. Kelsey, A.J. Bingham, E.P. Montgomery, E. D. Bennet, H.E. Potts, D.C.E. Rutherford, D.A. McDowell, D.A. Diver, D. Mariotti, Controlled microdroplet transport in an atmospheric pressure microplasma, *Appl. Phys. Lett.* (2015) 106, <https://doi.org/10.1063/1.4922034>.
- [34] J. Karthikeyan, C.C. Berndt, J. Tikkanen, S. Reddy, H. Herman, Plasma spray synthesis of nanomaterial powders and deposits, *Mater. Sci. Eng. A* 238 (1997) 275–286, [https://doi.org/10.1016/S0921-5093\(96\)10568-2](https://doi.org/10.1016/S0921-5093(96)10568-2).
- [35] Y.M. Su, Y.L. Kuo, C.M. Lin, S.F. Lee, One-step fabrication of tetragonal ZrO<sub>2</sub> particles by atmospheric pressure plasma jet, *Powder Technol* 267 (2014) 74–79, <https://doi.org/10.1016/j.powtec.2014.07.004>.
- [36] C. Luhrs, J. Phillips, P.T. Fanson, Production of complex cerium - aluminum oxides using an atmospheric pressure plasma torch, *Langmuir* 23 (2007) 7055–7064, <https://doi.org/10.1021/la063108m>.
- [37] J. Hong, Atmospheric Pressure Plasma Chemical Deposition By Using Dielectric, University of Illinois at Urbana Champaign, 2013. M. Sc. thesis.
- [38] H.H. Elsentriecy, K. Azumi, H. Konno, Effects of pH and temperature on the deposition properties of stannate chemical conversion coatings formed by the potentiostatic technique on AZ91 D magnesium alloy, *Electrochim. Acta.* 53 (2008) 4267–4275, <https://doi.org/10.1016/j.electacta.2008.01.009>.